Tina Memo No. 2002-001
Internal Report

Absolute reproducible quantification of Net Cerebral Blood Flow using Dynamic Susceptibility Contrast Enhanced MRI, and its application in disease

M.L.J. Scott, N.A. Thacker, P.A. Bromiley and A. Jackson

Last updated
8 / 12 / 2003

Imaging Science and Biomedical Engineering,
School of Cancer and Imaging Sciences,
University of Manchester, Stopford Building,
Oxford Road, Manchester M13 9PT, U.K.

Absolute reproducible quantification of Net Cerebral Blood Flow using Dynamic Susceptibility Contrast Enhanced MRI, and its application in disease

M.L.J. Scott, N.A. Thacker, P.A. Bromiley and A. Jackson
Imaging Science and Biomedical Engineering,
School of Cancer and Imaging Sciences,
University of Manchester, Stopford Building,
Oxford Road, Manchester M13 9PT, U.K.
neil.thacker@manchester.ac.uk

1 Abstract

A novel analysis technique for the quantification of net cerebral blood flow using dynamic susceptibility contrast-enhanced magnetic resonance imaging is presented. The method is based on the spatial differentiation of the first pass time of arrival of the imaged contrast in each voxel to obtain the net mean transit time of contrast across a voxel and as such avoids the need for measurement of an arterial input function. The reproducibility of the technique is quantified for four normal subjects (mean age 39.8 years, range 33-46) yielding typical mean flows of 40-60 ml/100g/min in grey matter and 20-32 ml/100g/min in white matter. A statistical method for separating disease groups from normals using regional blood flow, based on the concept of vascular territories, is proposed and tested in a group of 64 normals (mean age 70.9 years, range 33-87) and 9 patients with Alzhiemer's Dementia (mean age 61.6, range 54-72). The two groups are highly significantly different using this method. The novel method produces flow values comparable to those obtained using PET and arterial spin labelling and the regional analysis has potential diagnostic utility.

Key Words: MRI, Perfusion, Vascular Territories, Probability reflattening.

2 Introduction

The measurement of Cerebral Blood Flow (CBF) using magnetic resonance imaging has been a subject of intensive research. Two methods are currently in common use. The first, dynamic susceptibility contrast enhanced magnetic resonance imaging (DSCE-MRI) uses dynamic imaging during the passage of of a bolus of paramagnetic contrast media to produce flow related signal changes. The second, arterial spin labelling (ASL) attempts to quantify perfusion by measuring the in-flow of protons into the imaged slice over a set time period. DSCE-MRI remains the most commonly used, particularly in the clinical setting because of the simplicity of the scanning sequences and data acquisition. However, the calculation of cerebral blood flow values using conventional models has been shown to be subject to significant errors which restrict the use and interpretation of the technique. This paper will describe the analysis technique for the calculation of cerebral blood flow from DSCE-MRI data based on a recently described alternative physiological model of blood flow.

2.1 Conventional Analysis Techniques

Using the Central Volume theorem [23], CBF is defined as the ratio of Cerebral Blood Volume (CBV) to Mean Transit Time (MTT). The definition of CBV is unambiguous and the area under the first pass of the bolus concentration time-course curve gives a relative measure of this quantity. This relationship appears to hold well across a wide range of vessel sizes [1].

The definition of MTT has been taken [8] to mean the time taken for blood to pass from the arterial to venous blood pool. Using this definition, MTT is independent of the imaged voxel dimensions, since the quantity measured is the time taken to traverse the capillary network [18]. In early DSCE-MRI work MTT was calculated as the width of the contrast concentration residue function, until it was realised that this width is greatly influenced by contrast dose, injection rate and cardiovascular function [17]. In order to overcome these problems, the voxel residue function is deconvolved with the voxel arterial input function (AIF) to obtain MTT, generally using techniques such as Singular Value Decomposition (SVD) [14][15] or the Fourier Transform [21].

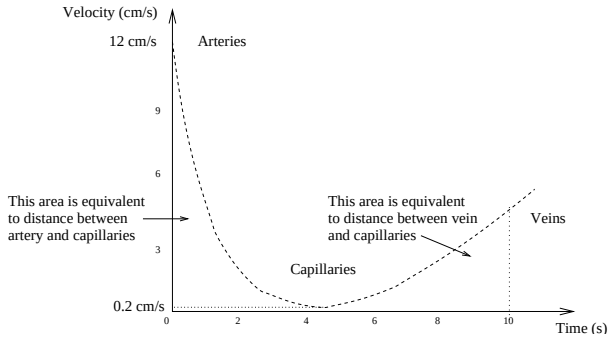

Figure 1: Diagram illustrating the typical passage of a molecule of contrast agent through the brain vasculature, entering the system in the arteries at ≈12cm/s, dropping to a velocity of ≈0.2cm/s in the capillaries and exiting through the veins at ≈6cm/s. The total distance travelled by the molecule is equivalent to the area under the graph.

This computational process defines the MTT as the voxel residence time and will reflect the observed passage of blood through the arterial, capillary and venous components within the measurement volume. If there is any variation in the time at which blood arrives at different points within the measurement space due to delay within the arterial tree, then this measurement of MTT will be dependent on voxel geometry: the larger the voxel, the longer the blood will remain within it.

MTT will be independent of voxel dimensions only if the observed drop in MR signal intensity occurs solely as the result of contrast agent in the true capillaries and therefore reflects the transit of contrast from arterial to venous blood pools. However, as noted above, signal drop is observed for all vessel sizes. In this paper we will therefore work with a definition of MTT that is directly equivalent to voxel residence time in order to be consistent with the observed behaviour of the data.

It is impracticable to find the true voxel AIF, as this requires specific knowledge of the shape of the distribution as it enters the measurement voxel. Instead a surrogate AIF from a major basal artery, typically the middle cerebral artery, is used. This technique suffers several drawbacks, as described in more detail elsewhere [29][28][4]. Delay and dispersion effects will occur between the artery in which the AIF is measured and the voxel being investigated such that the AIF no longer represents the voxel input function. This will be particularly true in small vessel occlusive diseases such as arthritides and moyamoya syndrome [5] where broad variations in arterial blood delivery time are seen. Calamante et. al. [4] describe the potential errors introduced by broadening a bolus by 2.5 seconds, amounting to an overestimation of MTT by 200% and underestimation of CBF by 50%. It has also been observed [21] that delay introduces further errors in the estimation of the residue function when deconvolution is attempted using SVD.

DSCE images may be acquired using either gradient or spin echo sequences. Early workers favoured spin-echo acquisitions since they produce signal changes which are more dependent on contrast passage through small vessels and were therefore felt to be more "capillary specific". In practice however, contrast passage through large vessels can still be seen and is indeed essential if an AIF is to be derived. Furthermore, the use of spin-echo decreases the signal to noise ratio in the acquisitions and may require the use of increased doses of intravenous contrast. Simonsen et al. [19], Marstrand et al.[10] and Speck et al.[22] have compared the use of spin-echo and gradient-echo acquisition sequences. Simonsen et al. [19] have shown no effective differences in the measured values of blood volume and blood flow, whereas Marstrand et al.[10] and Speck et al.[22] recommend the use of gradient-echo sequences for DSCE-MRI in preference to spin-echo sequences. The choice of sequence impacts on the analysis process. If spin-echo images predominantly reflect signal change in small vessels then the AIF measured in the basal artery can only be a relative value and it is not possible to obtain an absolute perfusion value. Gradient-echo acquisitions accurately reflect the contrast contribution of large vessels, but now the assumption that the measured signal change principally reflects contrast passage through the capillaries is invalid and estimated values of perfusion and MTT will become increasingly dependent on voxel geometry.

Conventional analysis methods are therefore subject to three major generic problems. First, it is not possible to derive an accurate AIF for each individual voxel, secondly, the MTT cannot be measured reliably and thirdly, flow cannot be measured absolutely. Each of these problems arises from the use of a physiological model of blood flow which is based entirely on non-directional flow in each voxel as a basis for analysis.

2.2 Measurement of Net Cerebral Blood Flow

We have recently tested an alternative physiological model of blood flow through the brain which could be applied to implement a novel approach to the measurement of blood flow from DSCE-MRI data [26]. This model assumes that all flow through an individual voxel can be treated as directional in nature. Although true capillaries (at the site of nutrient exchange) are tortuous and random in orientation they represent only a small component of the vascular tree (see fig. 1), having an average length of under 0.05cm. These true capillaries are fed by larger transit capillaries, which feed from the arterioles and into the venules of the main vascular tree. The transit capillaries and larger vessels are directional in nature, so that at the spatial scale of a voxel a net flow process can be hypothesised which will reflect the true total blood flow to the voxel. We have tested this physiological model in a previous publication by comparing directly measured net flow velocities in individual voxels derived from DSCE-MRI with values predicted by the model based on known physiological parameters. The velocities of 0.25 and 0.21 cm.s^{-1} measured using DSCE-MRI in grey and white matter agreed closely with predicted values of 0.25 and 0.18 cm.s^{-1}.

3 Theory

The following section describes the novel analysis technique for the measurement of cerebral blood flow.

3.1 Image formation and fitting a Gamma Variate

The collection of DSCE data can be performed using a number of imaging sequences. However, the constrictions of the physiological model demand the use of isotropic voxels across the 3D volume. In order to conform to this restriction, we have adopted the use of an echo shifted segmented echo planar imaging technique, known as PRESTO [9], as used in Kassner et al. [7] and Thacker et al. [26].

The DSCE data produces one signal-time course curve for each voxel in the image. The logarithm of the fractional signal drop is proportional to the quantity of contrast agent present in the voxel as a function of time. Our analysis technique necessitates accurate and reliable estimation of the arrival time of a bolus in each voxel. The bolus curve is located within the data using a matched filter approach, which involves convolving the data with a set of normalised gamma-variate curves (the expected distribution) as a function of width and position. Peaks in this two-dimensional distribution generate candidate locations for the bolus. Fixed regions around these peaks are then fitted to a gamma-variate curve truncated at 20% of the peak height (following the peak) in order to remove the effects of recirculation.

3.2 Estimation of CBV and Bolus Arrival Time

The time of arrival parameters most commonly used are the time of arrival of the first contrast molecules (T0) and the time to peak of the contrast concentration curve (TTP). T0 is used on the basis that it is thought to represent the arrival of molecules which have not been delayed by bolus broadening, and therefore represents the true underlying flow process. TTP is used as it represents the point of arrival of the greatest concentration of contrast and is straightforward to estimate and robust in situations where the signal to noise ratio is low.

Since significant signal changes can be seen in vessels of all sizes it can be assumed that the concentration time curve represents the cumulative effects of all contrast molecules resident within the voxel at any given time. Therefore, the entire contrast distribution needs to be taken as indicative of the time at which a tissue is perfused. We use the average arrival time, the time to mean (TTM)

$$TTM \;=\; \frac{\int t\; G(\mathbf{P},t)dt}{\int G(\mathbf{P},t)dt} \tag{1}$$

where $\mathbf{P}$ is the set of fitted parameters for the gamma variate G. TTM has been shown to exhibit a much smoother distribution than T0 or TTP and is not adversely affected by quantisation of the temporal fitting parameters [27].

We have previously shown in [26], using 2D and 3D temporal representations, that the passage of contrast agent through the brain can be considered (locally) as a wave front passing across the brain. There is a net flow component through the voxel that can be observed using 3D spatial differentiation of the arrival time. We define the net (voxel) mean transit time (NMTT) as the change in arrival time in a direction perpendicular to this wave front

$$NMTT \;=\; \sqrt{(\Delta TTM_x)^2 \;+\; (\Delta TTM_y)^2 \;+\; (\Delta TTM_z)^2} \tag{2}$$

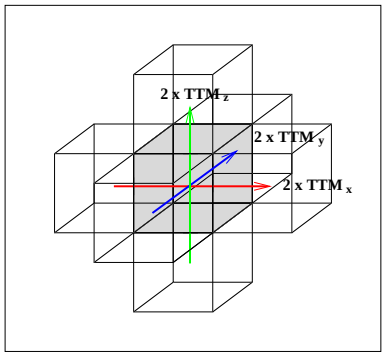

Figure 2: Diagram illustrating the differences in Time to Mean (TTM) in orthogonal directions across the (shaded) central voxel of interest.

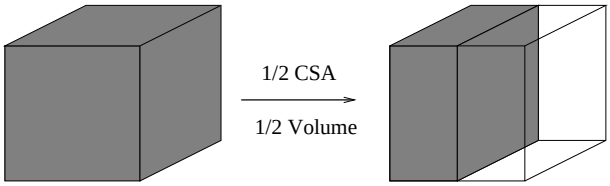

Figure 3: Diagram illustrating that, for a cube, a fractional cross-sectional area is equivalent to a fractional volume.

where the computed finite differences (ΔTTM_x etc.) illustrated in Fig. 2 correspond directly to the directional flow processes. A particular change in AIF distribution results only in a systematic shift in TTM (Appendix B) such that arrival times are invariant to global change in AIF. Importantly NMTT will also be invariant to change in the voxel input function provided that it is the same for adjacent voxels. Gradual changes in delay and dispersion effects will have no significant effect on the NMTT calculation.

The area under the gamma-variate curve gives a direct estimate of *relative* CBV (RCBV). Note that RCBV is also commonly used in the literature as an acronym for regional CBV. It is assumed that the relationship between the measured volume, RCBV, and true CBV is linear within the tissues of interest. However, by also assuming that the deviation from linearity is constant for a given imaging protocol it is possible to directly relate scaling between data sets. RCBV can be normalised using the value of a voxel which is 100% blood, i.e. a voxel in an artery or vein. This value can be obtained by assuming that the voxel exhibiting the highest value represents 100% blood. Automatic identification of such a voxel is difficult, as true arterial data are often surrounded by lower values and also cannot easily be distinguished from fit failures, which may be common. The approach taken here involves computing a maximum intensity projection (MIP) of the RCBV maps of every imaged slice to create an image in which large blood vessels produce linear structures. The MIP image is then filtered using a tangential smoothing operator, which applies interpolated smoothing at each voxel along the direction tangential to the local image slope. This technique is specifically designed to smooth along linear structures, such as large blood vessels, and to remove fit failures. Identification of the maximum RCBV value in the resulting image provides the scaling factor required for normalisation. Observation of the resulting distribution of values within normal brain data provides no evidence of a systematic error on the CBV [1](i.e. the volume to log-signal change relationship appears to hold well across the entire distribution of true blood volumes).

3.3 Flow Calculation

Physiological flow (perfusion) measures the volume of blood passing through an organ/tissue of known mass in a certain time and is measured in units of millilitres of blood per 100 grams of tissue per minute ($\mathrm{ml.100g^{-1}.min^{-1}}$). Here we are interested in the flow of blood in grey and white matter, so the conversion of voxel-based flow to the standard units involves the calculation of the equivalent flow that would be observed in a 100g volume of homogenous tissue. In physical systems, flow is defined as cross-sectional area (CSA) $\times$ velocity. For an isotropic cubic voxel, flow is not proportional to the volume of the voxel, but to volume$^{2/3}$, so the flow estimate cannot be converted to a perfusion value by a proportional volume scaling. In terms of the cross-sectional area, we require the cross-section of a cube of 100g brain tissue, scaled by the fraction of the blood passing through the cube, the CBV. Note that although CBV is a fractional *volume* measurement, because we are considering a cube of tissue,

the fractional volume is equivalent to the fractional cross-sectional area (see Fig. 3)

$$CSA = CBV \times \left(\frac{M}{\rho}\right)^{\frac{2}{3}} \tag{3}$$

where M is the mass (100g), ρ is the density of brain tissue, at 1.08g.cm^{-3}. Velocity (cm.min^{-1}) can be calculated as

$$velocity = \frac{60 \times l_{vox}}{NMTT} \tag{4}$$

where l_{vox} is the length of the voxel in cm, NMTT is the Net Mean Transit Time in seconds.

3.4 Error Modelling

For any calculation to be meaningful, it is necessary to quantify the errors on the calculation. Only then is it possible to determine whether an observed difference in the measurement represents genuine change. The calculation of NCBF (and production of the CBV and NMTT maps) results in statistical error distributions that vary according to the measurement. Appendix A explains the error model we assume and how it has been calibrated using repeatability experiments. Systematic errors on NCBF, if used as a surrogate for perfusion, will depend upon the definition of perfusion adopted. We claim here only that NCBF can therefore be expected to have utility in decision support and patient management.

4 Methods

4.1 Subjects and Scan Details

The study was approved by the Central Manchester Local Research Ethical Committee and all subjects gave informed consent for inclusion in the study. Scans were performed on 64 normal subjects (male = 24 mean age = 70.9, range = 33-87 years), with repeat scans in four of the male subjects (mean age = 39.8, range = 33-46 years). Scans were also performed on 9 individuals with Alzheimer's Dementia (male = 2, mean age = 61.6, range 54-72 years). All volunteers gave informed consent prior to inclusion. Imaging was performed using a 1.5 Tesla whole-body scanner (Philips ACS PT 6000 NT, Philips Medical Systems, Best, The Netherlands) with a quadrature birdcage head coil. The radiographer took care to align the scans of all patients in a consistent manner, using the longitudinal fissure to constrain the brain in the sagittal plane. Slices were then imaged parallel to a plane orthogonal to this, defined by the axis running through the anterior and posterior commisures. All subjects underwent an axial T1 inverse recovery scan (TR=6850ms, TE=18ms, TI=300ms, echo train length = 9, slice thickness = 3mm, matrix = 256×204, FOV=230×184mm, 51 contiguous slices) to obtain anatomical images for grey and white matter segmentation, as well as the MR DSCE imaging using PRESTO [9](TR=20ms, TE=28ms, Flip Angle = 10° , EPI factor = 9, matrix size=64^2, voxel size = 1.80×1.80×3.0mm for the normals (and one Alzheimer's patient) and 3.5mm for the rest of the Alzheimer's group. Here, 25 spatially contiguous slices are acquired over 40 time points at a temporal resolution of 1.9s. Contrast agent (0.1mM/kg of body weight; Gd-DTPA-BMA, Omniscan, Nycomed Uk, Ltd., Little Chalfont, UK) was injected intravenously during image acquisition as a bolus of 4 seconds duration, followed by a chaser of 20-30 mL of normal saline at the same rate. Injections were made using a Medrad power injector (Spectris MR injector, Medrad, PA). Imaging data were transferred to an independent workstation for analysis using the TINA suite of tools (http://www.tina-vision.net).

In the case of the 4 subjects who underwent the repeated scans, both the original and repeat scans were carried out between 8:30am and 11am. The repeat scans were taken between 4 and 21 days apart, and the subjects were advised to avoid the consumption of alcohol the night before and caffeine on the morning of the scans and to eat as normal.

4.2 Image Analysis

Cerebral Blood Flow measurements were performed as described above. Flow calculations were only performed in one slice of the brain, at the level of the upper border of the third ventricle. Image coregistration was performed between the original and repeat scans of the four subjects in whom repeat scanning had been performed. Registration of images obtained during each individual time course acquisition was unnecessary and accuracy of radiographic positioning was sufficient to provide equivalent slice locations in different subjects.

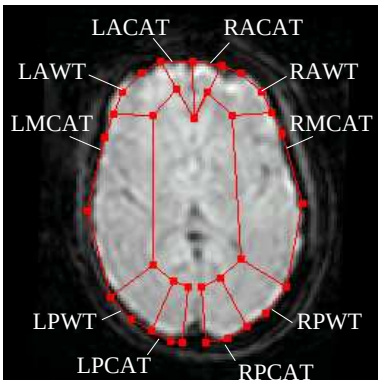

Figure 4: The vascular territories overlaid on a T2* map at the level of the upper border of the third ventricle. L/R = Left/Right, A/M/PCAT = anterior/middle/posterior cerebral arterial territories, A/PWT = anterior/posterior watershed territories.

The RCBV images are ideal for registration as they show high contrast between the bright large vessels and dark tissue, and also show the underlying structure of the major vessels, which is fairly rigid and should not differ in position between the two scans, although may well change in intensity. Use of the RCBV images instead of the raw T2* images displaying the maximum contrast avoids any problems due to temporal misplacement of the bolus. The RCBV volumes for the two datasets were calculated and registered and the registration parameters were applied to the T2* raw images in preparation for producing the parametric maps.

The TTM maps have of the order of 1% fit failures. A 3D median filter can be applied to the images in order to eliminate these. Median filtering involves replacing each voxel with the median value from the adjacent voxels and is used frequently in image processing tasks as a minimally destructive method for removing outlier data.

The anatomic axial T1 inverse recovery images were manually registered to the dynamic PRESTO scans, since automatic registration was difficult due to the completely different contrast in the two image sets. Segmentation of anatomical images into grey matter, white matter and cerebrospinal fluid was performed using a Bayesian segmentation approach [16] to produce probability maps of tissue distribution. These probability maps were thresholded at 0.5 to produce masks of grey and white matter, which were used to segment the parametric maps. Average values of the parameter maps were then calculated for grey and white matter.

4.3 Practical Use of Net Cerebral Blood Flow

Having developed a method for quantifying blood flow parameters, it is necessary to show that they can be of clinical or diagnostic use in investigating cerebrovascular disease. It is known that in normals subjects under normal conditions, different regions of the brain are supplied by specific and different arteries. These regions should therefore exhibit different flows and these flow differences might change systematically in disease. There is known hypoperfusion in the brains of Alzheimer's Disease patients (particularly in the temporal lobes) [20] due to lack of demand. Therefore, by investigating the correlations in flow between different regions of the brain, we might be able to differentiate Alzheimer's Disease patients from normal subjects.

As illustrated in Appendix A, the NCBF distribution for a single slice through the brain is highly skewed due to the presence of a few high flow vessels. Application of a logarithmic transform makes the data more Gaussian and thus more suitable for quantitative use.

4.3.1 Vascular Territories

We have devised a method for separating the brain, at the level of the upper border of the third ventricle, to identify 10 areas which conform to the approximate distribution of classical[11] vascular territories. The arterial regions are those directly served by the anterior, middle and posterior cerebral arteries (left and right); the watershed regions (anterior and posterior) are those in between. An active shape model[6] defining control points is fitted to a representative T2* image using a linear affine transform and the regions are defined according to these points (Fig. 4).

The vascular territories are overlaid on the log NCBF maps and the mean and standard error of the pixel values in each of the 10 regions calculated. Note that the number of pixels in each of the regions varies enormously. The

Region	log(NCBF)	
	Avg. Mean	Avg. SE
RACAT	3.02	0.112
RAWT	2.65	0.078
RMCAT	2.89	0.042
RPWT	2.83	0.079
RPCAT	3.03	0.087
LPCAT	2.99	0.095
LPWT	2.74	0.084
LMCAT	2.91	0.043
LAWT	2.79	0.075
LACAT	3.14	0.113

Table 1: Means and Standard Errors of log NCBF for each region for the normal group. Regions are as given in fig. 4.

statistical error on the calculation of the mean of the log NCBF values in each of the regions is inversely proportional to the square root of the number of pixels in the region. The vascular territory data is high dimensional (10D), so we use Principle Components Analysis (PCA) to investigate the main modes of variation in the normal group, and in order to obtain the variances of the modes, which are required for "whitening" the distribution in preparation for null hypothesis tests. In statistical terms, PCA should be interpreted as a hyperplane fit. Data provided to it must therefore have the property of uniform variance in all dimensions of the measurement vector in order that the principle axes are determined correctly. This requires a scaling factor for each regional average of log NCBF.

In order to obtain the scale factors, the average of the regional standard errors over all of the normal data is calculated (see Table 1). Assuming hemispherically-symmetric flow processes, the average of the scale factors for opponent left and right regions can be taken. Singular Value Decomposition (SVD) is used to perform PCA on the covariance matrix of this scaled data space, giving the eigenvectors (the principle axes of a rotated vector space) and the eigenvalues. Interpretation of the results from such an analysis requires an understanding of the contribution of statistical noise to the eigenvector space. As the pattern-space has been normalised to the noise process, a unit change in measurement is at the level of 1 standard error. The contribution due to noise in the resulting eigenvector analysis can therefore be estimated using a Monte-Carlo of a pure 10 dimensional unit Gaussian noise model. This allows the determination of which eigenvectors are consistent with noise, and which account for the true variation in the data.

4.3.2 Normal and Alzheimer's Probability Distributions

The subject data is transformed into the eigenvector space, such that there is a 10D distribution of normals in the eigenvector space centred about a zero origin, with the variance on each axis equal to the eigenvalue. Having normalised the variance of each dimension to 1/2, the (1-sided) complementary error function can be used to determine, for each dimension in each subject, the probability that the rotated data value has been drawn from a Gaussian distribution. If the distribution of normals is consistent with a Gaussian distribution then, for each dimension, a histogram of the complementary error function values for those subjects will be uniform.

Probabilities from each dimension of the model can be combined using the "multiply and re-flatten" approach described in Appendix C [2]. Although such techniques are common in the area of statistics we believe that this general proof of the re-flattening relationship for arbitrary dimensional data is novel. Using this approach we can test the hypothesis that the Alzheimer's patient data are consistent with having been drawn from the same distribution as the normals. The null hypothesis for the entire Alzheimer's group can also be tested by multiplying these hypothesis probabilities across the group and applying the same re-flattening procedure. This one statistical approach thus gives the benefit of either individual or group-level statistical testing and does not require that the disease group also has a Gaussian distribution. This makes the technique suitable for use in all diseases, not just those which produce systematic shifts in measurement.

5 Results

First we describe the flow values and repeatability results from the four young normals with repeat scans, then go on to describe the results of applying the vascular territories method to the log-NCBF maps of the normals

Subject	Grey Matter		White Matter	
	1st Scan	2nd Scan	1st Scan	2nd Scan
1	0.082	0.097	0.058	0.068
2	0.079	0.073	0.061	0.053
3	0.066	0.083	0.039	0.052
4	0.097	0.102	0.040	0.053

Table 2: Mean RCBV values in grey and white matter for the original and repeat scans of the four repeated subjects.

Subject	Grey Matter		White Matter	
	1st Scan	2nd Scan	1st Scan	2nd Scan
1	0.64	0.61	0.67	0.68
2	0.60	0.68	0.74	0.77
3	0.65	0.65	0.85	0.81
4	0.57	0.68	0.65	0.69

Table 3: Mean NMTT values in grey and white matter for the original and repeat scans of the four repeated subjects.

Subject	Grey Matter		White Matter		Grey:White	
	1st Scan	2nd Scan	1st Scan	2nd Scan	1st Scan	2nd Scan
1	41.2	56.8	24.2	31.7	1.7	1.8
2	45.7	41.9	28.6	27.1	1.6	1.5
3	34.4	40.0	16.4	20.4	2.1	2.0
4	58.7	51.6	20.5	21.4	2.9	2.4

Table 4: Mean NCBF values in grey and white matter for the original and repeat scans of the four repeated subjects. Grey/white matter ratios for the two scans are also given.

and Alzheimer's patients and to look at the probability that these two groups have been drawn from the same distribution.

5.1 Grey and White Matter Results

Table 2 illustrates that the average grey matter RCBV = 0.085, and the average white matter RCBV = 0.053. This is in reasonable agreement with the values used in [26]. These values are not the blood volume in the true grey/white matter capillaries, as assumed in the physiological model of [26] but, due to the approximately linear relationship between log signal drop and contrast density, are the average blood volume of all vessels in the grey/white matter.

The average NMTTs across a voxel of length 1.80mm in grey and white matter are 0.64s and 0.70s respectively, corresponding to net voxel velocities of 0.28 cm.s^{-1} and 0.26 cm.s^{-1}.

The average values for NCBF are 46.3 and 23.8 ml.100g^{-1}.min^{-1} for grey and white matter respectively. The ratios of grey:white matter NCBF are quite variable over the four subjects, yet consistent within each subject.

5.2 Error Modelling

Table 5 gives, for each subject and each TTM slice used in the calculation of the NMTT, the error on the pixels of that map for both the raw TTM maps and the TTM maps after 3D median filtering. There is an improvement in statistical error of approximately three times following filtering. This improvement is significant and provides data of sufficient accuracy for reliable determination of NMTT.

Table 6 gives the error for the $\sqrt{RCBV}$ and NMTT maps. The error on the $\sqrt{RCBV}$ corresponds to approximately 5%. The error on the NMTT corresponds to approximately 20%. Figure 5 shows a Monte-Carlo noise distribution at this error level overlaid on the NMTT distribution, illustrating that for typical measured values of NMTT the noise is small, and that the data is noisiest for low transit times. Measurements of NMTT less than 0.5s are entirely consistent with noise and will include all data in large blood vessels.

Subject	Slice	σ_{TTM}	σ_{MedTTM}
1	1	0.585	0.181
	2	0.603	0.189
	3	0.640	0.184
2	1	0.697	0.192
	2	0.641	0.192
	3	0.742	0.201
3	1	0.656	0.194
	2	0.782	0.200
	3	0.879	0.200
4	1	0.556	0.172
	2	0.610	0.179
	3	0.640	0.188

Table 5: Errors on the three TTM maps and median filtered TTM maps (used to create the NMTT maps) for each of the four repeated subjects. Note the three-fold improvement in statistical accuracy following median filtering.

Subject	RMS $\sigma\sqrt{RCBV}$	σ_{NMTT}
1	0.0114	0.142
2	0.0113	0.156
3	0.0142	0.162
4	0.0107	0.134

Table 6: Errors on the $\sqrt{RCBV}$ and NMTT maps for the four repeated subjects.

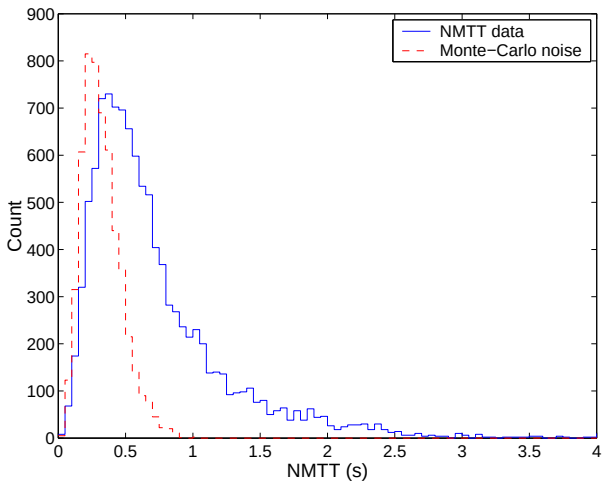

Figure 5: Histogram of typical NMTT data for a slice overlaid with the corresponding Monte-Carlo noise distribution. Measurements of NMTT less than 0.5s correspond to data from large vessels and are consistent with noise.

In order to make best use of these data it is important to have a quantitative understanding of the statistical error processes for NCBF in various tissues. The statistical error model presented in Appendix A can be used with the parameters specified above for this purpose. Using the worst case values of $\sigma_{NMTT} = 0.162$ and $\sigma_{\sqrt{CBV}} = 0.0142$ as fixed values in the σ_{NCBF} and $\sigma_{logNCBF}$ calculations, keeping CBV at three fixed levels of 0.03 (representing white matter), 0.08 (grey matter) and 1.0 (large artery or vein), assuming that NCBF $\propto$ RCBV/NMTT, and that (based on typical observed values) white matter flow ranges from 5-50 ml.100g^{-1}.min^{-1}, grey matter flow from 10-150 ml.100g^{-1}.min^{-1} and arterial flow from 150-1000 ml.100g^{-1}.min^{-1}, then Figs. 6(a) and 6(b) illustrate the absolute NCBF and absolute log NCBF error as a function of log NCBF.

Figure 6(a) illustrates that for a given RCBV and over the range of flow we are interested in, the larger RCBV vessels (displaying a greater flow) have a much greater error. As the error on the flow is not constant across the whole range of NCBF this data is unsuitable for computation of a simple mean flow value. Such an estimate would be dominated by unstable large values. Figure 6(b) shows the error on the log NCBF maps against log NCBF, and this shows that, over the range of log NCBF expected in these vessels, there is a reasonably uniform range of

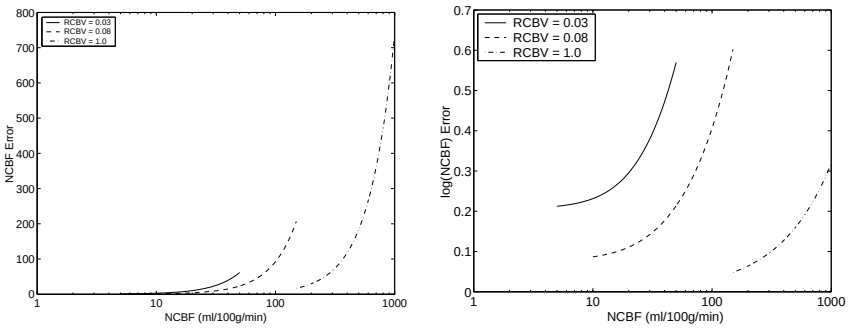

(a) NCBF error vs log NCBF. (b) Log NCBF error vs log NCBF.

Figure 6: Error distributions of log NCBF.

Regions	RACAT	RAWT	RMCAT	RPWT	RPCAT	LPCAT	LPWT	LMCAT	LAWT
RACAT	1.0	-	-	-	-	-	-	-	-
RAWT	0.72	1.0	-	-	-	-	-	-	-
RMCAT	0.53	0.59	1.0	-	-	-	-	-	-
RPWT	0.23	0.57	0.50	1.0	-	-	-	-	-
RPCAT	0.46	0.57	0.63	0.42	1.0	-	-	-	-
LPCAT	0.48	0.57	0.71	0.54	0.69	1.0	-	-	-
LPWT	0.33	0.39	0.44	0.61	0.49	0.63	1.0	-	-
LMCAT	0.60	0.61	**0.78**	0.61	0.65	0.70	0.54	1.0	-
LAWT	0.60	**0.88**	0.63	0.62	0.63	0.62	0.37	**0.75**	1.0
LACAT	0.56	0.76	0.62	0.46	0.56	0.49	0.28	0.66	**0.77**

Table 7: Correlation Matrix of the weighted Normal log(NCBF) data for the ten vascular regions (correlation of LACAT with itself omitted).

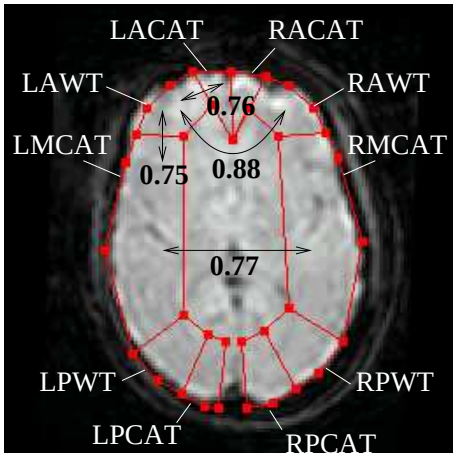

Figure 7: Diagram showing the four highest correlations between regions, arrows indicate correlations, numbers give correlation value.

statistical error. The mean log NCBF is therefore used for as the summary variable for each region. It is important to note that this weighting process implicitly reduces the significance of large blood vessels without the need for techniques such as thresholding, which can lead to problems in reproducibility.

5.3 Vascular Territories

Table 5.3 shows the matrix of the mean log NCBF values of the ten vascular territories. The four greatest correlations between regions are shown in Fig. 7. These correlations illustrate two features of the data. First, there are high correlations between symmetrical regions of the brain: left and right anterior watershed and left

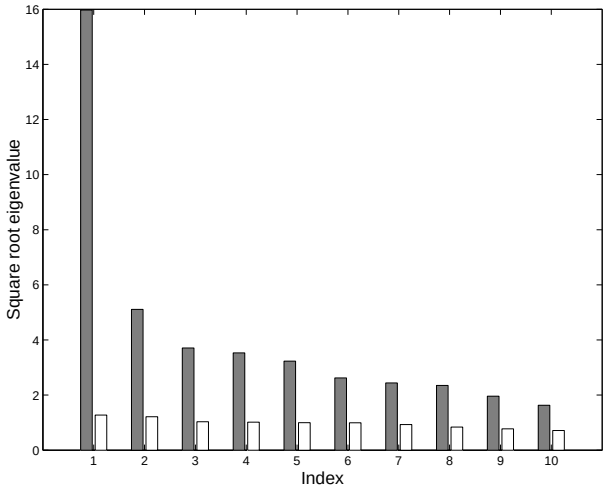

Figure 8: Histogram of $\sqrt{eigenvalues}$ for the Normals plus Monte-Carlo simulation of noise

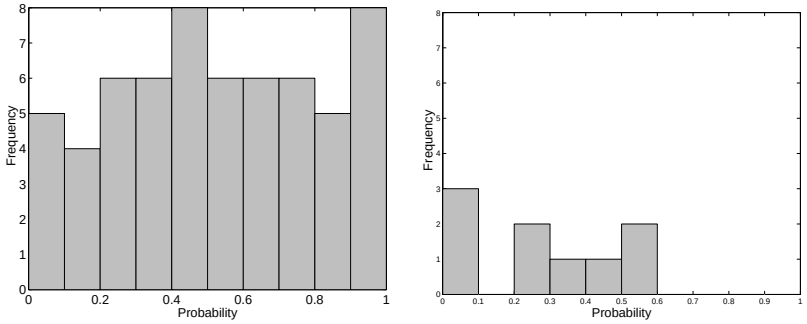

(a) (b)

Figure 9: Histogram of reflattened probability values for (a) normals and (b) Alzheimer's subjects.

and right middle cerebral artery territories. This indicates that the physiological mechanisms involved in flow generation are symmetric. Second, there are also high correlations between the left anterior watershed territory and the adjacent two arterial territories. This is unsurprising, as the watershed territory might be expected to be fed by the arteries feeding the adjacent arterial regions.

Figure 8 shows the square root of the eigenvalues for the 10 eigenvectors derived using PCA on the 10 vascular territories for the normals. A Monte-Carlo simulation of the noise is also shown. PCA should ideally result in a reduced representation of the data. Although there is some evidence that the later eigenvalues in the model are converging on the noise, there is no clear separation of the signal and noise components. Some information regarding measurable normal variation is present even at the 10th component, which suggests that this model of normal variation is not compact and that none of the eigenvectors can be discarded.

5.3.1 Hypothesis Testing for Individuals and Groups

All of the square root eigenvalues exceed the Monte-Carlo noise, therefore none of the eigenvector dimensions were discarded, all ten probability values were combined and the result reflattened (see Appendix C). For the normal subjects, the probability distributions for all ten dimensions were not significantly different from flat (using 10 bins from 0 to 10, degrees of freedom = 9, at the p = 0.05 level) indicating that all the dimensions are drawn from the normal distribution.

Figures 9(a) and 9(b) show the histograms of the reflattened probability values for the normals and Alzheimer's subjects. The histogram of normals is not significantly different from flat ($\chi^2 = 2.3$ df $= 9$). There are insufficient numbers of Alzheimer's patients to perform a Chi-square test. However, the same group hypothesis can be tested using the probability re-flattening technique, giving a probability of 7.4×10^{-5} that the entire Alzheimer's group was drawn from the same multi-dimensional Gaussian as the normal controls. Performing the same reflattening technique on the normal group results in a p-value of 0.54. This is consistent with the histogram of the normal

probabilities being uniform, as data less flat than this would be generated by the assumed model 54% of the time.

6 Discussion and Conclusions

This paper introduces a method for the quantification of a novel quantity; the Net Cerebral Blood Flow (NCBF). We have previously demonstrated that, except for the smallest capillaries, the movement of blood in the many vessels in a voxel can be considered as coherent, resulting in a net directional flow process through the voxel. The linear relationship between contrast concentration and log-signal change across the spectrum of vessel sizes (being particularly true for the PRESTO sequence used in the acquisitions) means that there is no significant preferential sensitivity to contrast in the capillaries and we must be observing the flow processes in vessels of all sizes.

The average NMTT values for the four repeated normals are slightly higher than expected. This may be due to the presence of larger vessels in the averaged regions (the regions of interest here and in [26] are not the same), and may also be due to the fact that young normals have been imaged here and might be expected to show a higher flow [30][3]. The NCBF values are in reasonable agreement with results from ^{15}O H_2O PET [31] of 67 and 33 ml.100g^{-1}.min^{-1} and ranges [12] of 25-80 and 11-35 ml.100g^{-1}.min^{-1}, and Arterial Spin Labelling (ASL) [31]; 64 and 23 ml.100g^{-1}.min^{-1} for grey and white matter respectively. In general, the grey and white matter values for RCBV, NMTT and NCBF are consistent with values expected from the physiology literature and from studies based on PET and spin-labelling. Note that in segmenting grey and white matter we have not removed the effects of larger vessels. The vessel size distribution is a continuum, so producing an accurate threshold for removal of large vessels in order to observe only the capillaries would be difficult. In addition, we do not have the spatial resolution to achieve this: one voxel will contain a variety of vessel sizes and partial volume effects. Another potential problem that has not been dealt with here is the effect of the difference in haematocrit between the macrovasculature and capillaries. The haematocrit in the larger vessels is greater than in the capillaries. As such, there will be more plasma and hence a higher concentration of contrast in the capillaries compared to the larger vessels. Most groups (e.g. [14][13]) generally ignore the issue, or use one value for the ratio. However, the difference between the small and large vessel haematocrit values will vary according to the size of the vessels and the physiological attributes of the scanned subject, so a single scale factor across a whole group is probably inadequate. Ignoring the haematocrit may result in an overestimation of the RCBV (hence NCBF) in the capillaries and/or an underestimation in the larger vessels. The potential extent of this effect is unknown.

Using the current method for RCBV normalisation, a 5% error on the $\sqrt{RCBV}$ maps is achieved. This error will mainly be composed of true physiological change and inaccuracy in RCBV normalisation, since the registration and reslicing of the repeat scan to the original was accurate to within a fraction of a voxel. With the current scan parameters, a 20% error on the NMTT is the best that can be achieved. Here, the most severe limitation is the accuracy of the TTM maps, which is dependent on the temporal resolution of the data acquisition. Advances in scanner and sequence technology mean that we should be able to double the temporal resolution of data acquisition in the near future. The reproducibility between repeat scans of the same person is sufficient for 20% accurate quantification of NCBF at the voxel level, which can be reduced by spatial averaging. NCBF itself is not suitable for quantitative use, since the NCBF distribution is highly skewed and the errors on the NCBF are not uniform over the range of flow we wish to image. We have shown that the statistical error on the log NCBF is approximately uniform for the tissues we wish to measure in the brain, and that the log NCBF distribution approximates a Gaussian. This makes the estimation of a mean summary variable viable.

There are implications regarding the interpretation of identified regional correlations (Table 5.3) as these correspond to linear correlations between log NCBF values and not NCBF. Our analysis using PCA (effectively a hyperplane fit) suggests that the correlations between vascular regions are not compactly given in this representation. However, if there were good reason to think that correlations between regions might be linear in some other domain this would require the development of a purpose designed statistical analysis to replace PCA. Our current analysis has the advantage of whitening the distribution of the normal group, thus supporting the construction of a multivariate Gaussian hypothesis test. We have described a novel and general technique for the construction of such tests in this paper.

The histogram of the reflattened probability values shows that there are no Alzheimer's disease patients in the bins above p=0.6. This is insufficient for subject-by-subject decision support and is a direct consequence of the high degree of overlap between this group and the normal control subjects. However, we have demonstrated that using a group level comparison it is possible to demonstrate a statistically significant difference between the normals and Alzheimer's group. We have chosen here to concentrate on the individual and group level differences between the Alzheimer's patients and the normal group. The use of the vascular territories means that we could also make regional comparisons between the Alzheimer's and normal groups.

It is highly important to ensure that subjects in a longitudinal study are in the same physiological condition during each scan, and perhaps more importantly to ensure that all individuals in a cross-sectional study are in a similar state. This involves not only regulating the consumption of food and drink, but also ensuring that the subjects are comfortable and not stressed before and during the scan procedure, something which is difficult to achieve due to the presence of the intravenous cannula and noisy scanner. This is an area which we intend to investigate more systematically in future studies. However, the results presented here are sufficient to illustrate group level differences and confirm once a vascular involvement in Alzheimer's disease.

We have demonstrated that it is possible to quantify Net Cerebral Blood Flow with DSCE-MRI using a method based on the spatial differentiation of the arrival time of contrast in a voxel. The method avoids all of the problems of deconvolution and determination of an AIF. We have shown that the method produces results which are consistent with values obtained using other modalities such as PET, and quantified the errors on the calculated estimates. The technique has promise in the separation of groups with cerebrovascular disease from normals.

7 Acknowledgements

The authors would like to thank Prof. P Rabbitt for the use of data from 26 of the normal subject group.

References

[1] J L Boxerman, B R Rosen, and R M Weisskoff. Signal-to-noise analysis of cerebral blood volume maps from dynamic NMR imaging studies. *J. Magn. Reson. Imaging*, 7(3):528–537, May-Jun 1997.

[2] P A Bromiley, N A Thacker, M L J Scott, M Pokrić, A J Lacey, and T F Cootes. Bayesian and non-Bayesian probabilistic models for image analysis. *Image Vision Comput.*, 21:851–864, 2003.

[3] P C Buijs, M J Krabbe-Hartkamp, E E de Lange, L M P Ramos, M M B Breteler, and W P T M Mali. Effect of age on cerebral blood flow: Measurement with ungated two-dimensional phase-contrast MR angiography in 250 adults. *Radiology*, 209:667–674, 1998.

[4] F Calamante, D G Gadian, and A Connelly. Delay and dispersion effects in dynamic susceptibility contrast MRI: Simulations using singular value decomposition. *Magn. Reson. Med.*, 44(3):464–473, Sep 2000.

[5] F Calamante, V Ganesan, F J Kirkham, W Jan, W K Chong, D G Gadian, and A connelly. MR perfusion imaging in Moyamoya syndrome - potential implications for clinical evaluation of occlusive cerebrovascular disease. *Stroke*, 32:2810–2816, 2001.

[6] T F Cootes, A Hill, C J Taylor, and J Haslam. The use of active shape models for locating structures in medical images. *Image Vision Comput.*, 12(6):355–366, 1994.

[7] A Kassner, D Annesley, A Jackson, X P Zhu, and Y Watson. Dynamic contrast susceptibility imaging in enhanced cerebral tumors: Techniques for reducing relaxivity effects. In *Proc. ISMRM*, Missouri, Nov 1998.

[8] V G Kiselev. On the theoretical basis of perfusion measurements by dynamic susceptibility contrast MRI. *Magn. Reson. Med.*, 46:1113–1122, 2001.

[9] G Liu, G Sobering, J Duyn, and C T Moonen. A functional MRI technique combining principles of echo-shifting with a train of observations (PRESTO). *Magn. Reson. Med.*, 30:764–768, 1993.

[10] J R Marstrand, E Rostrup, S Rosenbaum, E Garde, and H B W Larsson. Cerebral hemodynamic changes measured by gradient-echo or spin-echo bolus tracking and its correlation to changes in ICA blood flow measured by phase-mapping MRI. *J. Magn. Reson. Imaging*, 14:391–400, 2001.

[11] T B Moller and E Reif. *Pocket Atlas of Cross-Sectional Anatomy CT and MRI*, volume 1; Head, Neck, Spine and Joints. Theime, 1994.

[12] L Ostergaard, P Johannsen, P Host-Poulsen, P Vestergaard-Poulsen, H Asboe, A D Gee, S B Hansen, G E Cold, A Gjedde, and C Gyldenstad. Cerebral blood flow measurements by magnetic resonance imaging bolus tracking: Comparison with $[^{15}O]H_2O$ positron emission tomography in humans. *J. Cereb. Blood F. Met.*, 18(9):935–940, Sep 1998.

[13] L Ostergaard, A G Sorensen, K K Kwong, R M Weisskoff, C Gyldenstad, and B R Rosen. High resolution measurement of cerebral blood flow using intravascular tracer bolus passages. Part II: Experimental comparison and preliminary results. *Magn. Reson. Med.*, 36(5):726–736, Nov 1996.

[14] L Ostergaard, R M Weisskoff, D A Chesler, and C Gyldensted. High resolution measurement of cerebral blood flow using intravascular tracer bolus passages. Part I: Mathematical approach and statistical analysis. *Magn. Reson. Med.*, 36(5):715–725, Nov 1996.

[15] J E Perthen, F Calamante, D G Gadian, and A Connelly. Is quantification of bolus tracking MRI reliable without deconvolution. *Magn. Reson. Med.*, 47:61–67, 2002.

[16] M Pokrić, N Thacker, M L J Scott, and A Jackson. Multi-dimensional medical image segmentation with partial voluming. In *Proc. MIUA*, pages 77–81, 2001.

[17] K A Rempp, G Brix, F Wenz, C R Becker, F Guckel, and W J Lorenz. Quantification of regional cerebral blood flow and volume with dynamic susceptibility contrast-enhanced MR imaging. *Radiology*, 193(3):637–641, Dec 1994.

[18] W G Schreiber, F Guckel, P Stritzke, P Schmiedek, A Schwartz, and G Brix. Cerebral blood flow and cerebrovascular reserve capacity: Estimation by dynamic magnetic resonance imaging. *J. Cereb. Blood F. Met.*, 18(10):1143–1156, Oct 1998.

[19] C Z Simonsen, L Ostergaard, D F Smith, P Vestergaard-Poulsen, and C Gyldensted. Comparison of gradient- and spin-echo imaging: CBF, CBV and MTT measurements by bolus tracking. *J. Magn. Reson. Imaging*, 12:411–416, 2000.

[20] G W Small, P V Rabins, P P Barry, N S Buckholtz, S T DeKosky, S H Ferris, S I Finkel, L P Gwyther, Z S Khachaturian, B D Lebowitz, T D McRae, J C Morris, F Oakley, L S Schneider, J E Streim, T Sunderland, L A Teri, and L E Tune. Diagnosis and treatment of Alzheimer disease and related disorders: consensus statement of the American Association for Geriatric Psychiatry, the Alzheimer's Association, and the American Geriatrics Society. *J. Am. Med. Ass.*, 278(16):1363–1379, 1997.

[21] A M Smith, C B Grandin, T Duprez, F Mataigne, and G Cosnard. Whole brain quantitative CBF and CBV measurements using MRI bolus tracking: Comparison of methodologies. *Magn. Reson. Med.*, 43(4):559–564, Apr 2000.

[22] O Speck, L Chang, M DeSilva, and T Ernst. Perfusion MRI of the human brain with dynamic susceptibility contrast: Gradient-echo versus spin-echo techniques. *J. Magn. Reson. Imaging*, 12:381–387, 2000.

[23] G N Stewart. Researches on the circulation time in organs and on the influences which affect it. Parts I-III. *J. Physiol.*, 15:1–45, 1894.

[24] N A Thacker, F J Ahearne, and P I Rockett. The Bhattacharryya metric as an absolute similarity measure for frequency coded data. *Kybernetica*, 34(4):363–368, 1997.

[25] N A Thacker and P A Bromiley. The effects of a square root transform on a Poisson distributed quantity. Tina Memo 2001-010, 2001.

[26] N A Thacker, M L J Scott, and A Jackson. Can dynamic susceptibility contrast magnetic resonance imaging perfusion data be analyzed using a model based on directional flow? *J. Magn. Reson. Imaging*, 17(2):241–255, February 2003.

[27] N A Thacker, M L J Scott, A J Lacey, and G J M Parker. Accurate estimation of contrast arrival in T2* susceptibility contrast imaging. In *Proc. ISMRM*, Hawaii, 2002.

[28] N A Thacker, X P Zhu, M Nazarpoor, C Moonen, and A Jackson. A new approach for the estimation of MTT in bolus passage perfusion techniques. In *Proc. MIUA*, pages 61–64, London, July 2000. BMVA.

[29] R M Weisskoff, D Chesler, J L Boxerman, and B R Rosen. Pitfalls in MR measurement of tissue blood flow with intravascular tracers: Which mean transit time? *Magn. Reson. Med.*, 29(4):553–559, Apr 1993.

[30] F Wenz, K Rempp, G Brix, M V Knopp, F Guckel, T Hess, and G van Kaick. Age dependency of the regional cerebral blood volume (rCBV) measured with dynamic susceptibility contrast MR imaging (DSC). *Magn. Reson. Imaging*, 14(2):157–162, 1996.

[31] F Q Ye, K F Berman, T Ellmore, G Esposito, J D van Horn, Y Yang, J Duyn, A M Smith, J A Frank, D R Weinberger, and A C McLaughlin. $H_2^{15}O$ PET validation of steady-state arterial spin tagging cerebral blood flow measurements in humans. *Magn. Reson. Med.*, 44:450–456, 2000.

A Error Modelling of NCBF

We treat the estimation of perfusion parameters as analogous to the estimation of parameters of the Gaussian distribution. The CBV is corresponds to the area under the graph (N), so has an error proportional to $\pm\sqrt{RCBV}$, i.e. effectively a Poisson random variable. Such variables can be transformed to a domain of equal variance by taking the square root [24][25]. This process can be visualised using scatter plots of the relevant variables.

A.1 Results

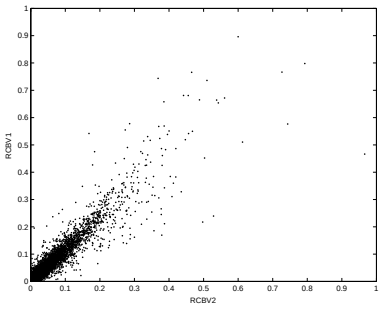

Figure 10: Scatterplot of $RCBV_1$ vs $RCBV_2$.

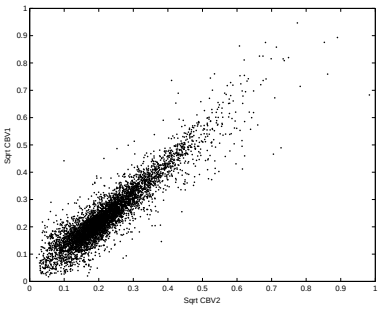

Figure 11: Scatterplot of $\sqrt{CBV_1}$ vs $\sqrt{CBV_2}$.

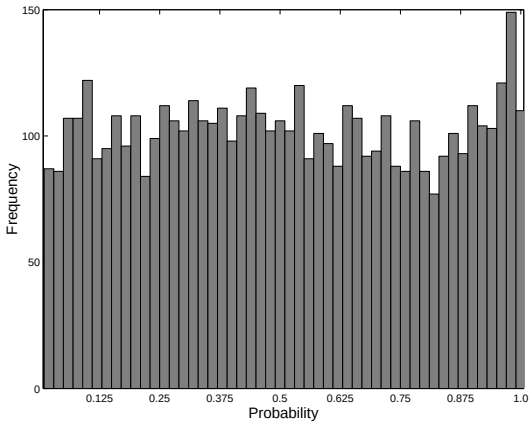

Figure 12: Error function distribution on $\sqrt{RCBV}$ difference map.

In order to validate our assumed error model, we can perform repeat measurements on the same subject, and compare the parameter maps. Fig. 10 shows a scatterplot of $RCBV_{scan2}$ vs $RCBV_{scan1}$ for the same normal. Fig. 11 shows the same for the $\sqrt{RCBV}$ maps. Note the uniform spread of the data in Fig. 11 as predicted if CBV were a Poison random variable. Fig. 12 shows the error function distribution of the $\sqrt{RCBV}$ difference map. Note the flatness of the histogram indicates that the error model is appropriate.

We can compare the original and repeat $\sqrt{RCBV}$ maps to obtain an estimate of the statistical error. The same can be done for the NMTT maps. In addition, we can demonstrate the NMTT error distribution by producing a Monte-Carlo simulation of the production of the NMTT maps using maps of noise, at the level of noise on the TTM maps. Having obtained the errors for the $\sqrt{RCBV}$ and NMTT maps ($\sigma_{\sqrt{RCBV}}$ and σ_{MTT} respectively) we can propagate these errors to estimate the statistical accuracy on a voxel in the NCBF map

$$\sigma_{NCBF} = \sqrt{\left(\frac{CBV}{NMTT^2}\right)^2 \sigma^2_{NMTT} + \frac{4CBV}{NMTT^2}\sigma^2_{\sqrt{CBV}}} \tag{5}$$

Note that due to the presence of a few high flow vessels and many low flow vessels, the distribution of NCBF is highly skewed (Fig. 13(a)).

We describe in the main text how we apply a logarithmic transform to make the distribution more Gaussian (Fig. 13(b)). When working in the natural logarithm scale, the estimated statistical error on the log NCBF is

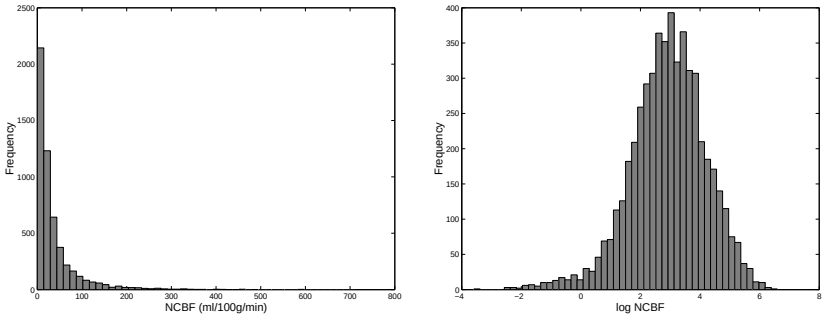

(a) NCBF (b) log NCBF

Figure 13: Illustrative distributions of NCBF and log NCBF.

$$\sigma_{logNCBF)} = \sqrt{\frac{\sigma^2_{\sqrt{CBV}}}{CBV^2} + \frac{\sigma^2_{NMTT}}{NMTT^2}} \tag{6}$$

These error models are sufficient to support quantitative statistical difference estimators on a per voxel basis.

B The Effects of Variable Arterial Input Functions on TTM.

We wish to show that a change in arterial input function (AIF) in a susceptibility perfusion experiment results only in a shift of coordinates on the observed Time to Mean (TTM).

We first define some useful quantities

$$TTM_{AIF} \;=\; \frac{\int t\; AIF(t)dt}{A_{AIF}}$$

$$TTM_{DT_v} \;=\; \int t\; DT_v(t)dt$$

where $DT_v(t)$ is the distribution of true arrival times at voxel v , and A_{AIF} is a constant of normalisation. The $DT(t)$ distribution is already normalised (i.e. $A_{DT} \;=\; 1$) as it is a probability distribution.

The observed contrast arriving at voxel v will be given by the convolution of the arterial input function and the arrival time distribution

$$C_v(\tau) \;=\; \int DT_v(t)AIF(\tau - t)\; dt$$

The estimated time of arrival for voxel v will be given by;

$$TTM_v \;=\; \frac{\int \tau\; C_v(\tau)\; d\tau}{A_{AIF}}$$

$$TTM_v \;=\; \frac{\int \tau\; \int DT_v(t)AIF(\tau - t)\; dt\; d\tau}{A_{AIF}}$$

We can now reorder the integration giving

$$TTM_v \;=\; \int DT_v(t)\; (\frac{\int \tau\; AIF(\tau - t)\; d\tau}{A_{AIF}})\; dt$$

Notice that the term in brackets is simply our earlier definition of TTM_{AIF} with a co-ordinate offset of t. Therefore,

$$TTM_v \;=\; \int DT_v(t)(t \;+\; TTM_{AIF})\; dt$$

$$=\; TTM_{AIF} \int DT_v(t)\; dt \;+\; \int t\; DT_v(t)\; dt$$

$$=\; TTM_{AIF} \;+\; TTM_{DT_v}$$

Thus changes in measured TTM due to change in the AIF distribution produce only systematic shifts in the origin of the coordinate system of TTM_{AIF} for all voxels. QED.

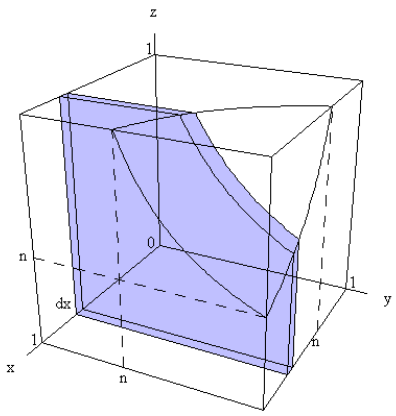

Figure 14: The sample space for the probability renormalisation in 3D, showing the element of integration (the shaded region) used to relate this to the 2D problem. The contour of constant probability is shown by the curved surface in the upper corner of the unit cube.

C Probability Renormalisation

Given n quantities each having a uniform probability distribution $p_{i=1,n}$, the product $p = \prod_{i=1}^{n} p_i$ can be renormalised to have a uniform probability distribution $F_n(p)$ using

$$F_n(p) = p \sum_{i=0}^{n-1} \frac{(-\ln p)^i}{i!} = p + p \sum_{i=1}^{n-1} \frac{(-\ln p)^i}{i!} \tag{7}$$

The quantities p_i can be plotted on the axes of an n dimensional sample space, bounded by the unit hypercube. Since they are uniform, and assuming no spatial correlation, the sample space will be uniformly populated. Therefore, the transformation to $F_n(p)$ such that this quantity has a uniform probability distribution can be achieved using the probability integral transform, replacing any point in the sample space p with the integral of the volume under the contour of constant p passing through this point, which obeys $\prod_{i=1}^{n} p_i = p = constant$. This can be expressed in terms of the volume of a hyper-region of one lower dimension by integrating over one dimension (let this be called x)

$$F_n(p) = p + \int_p^1 F_{n-1}(\frac{p}{x})dx \tag{8}$$

This is equivalent to dividing the integration into two regions using a plane perpendicular to the x axis that intersects the axis at $x = p$. Fig. 14 shows the element of integration that would be used in the 3D case, to relate the volume of the unit cube under the contour of constant probability to the 2D case.

Now, in the simplest case of $n = 1$, clearly $F_n(p) = p$, as no renormalisation is required. The solution for higher dimensions can then be derived by iterative application of Eq. 8. This involves integration of terms in $(p/x)[-\ln(p/x)]^n$ which enter in the n=3 and higher cases. This integration can be performed using a simple substitution $x = pu$, $dx = pdu$

$$\int_p^1 (\frac{p}{x})[-\ln(\frac{p}{x})]^n dx = p \int_1^{1/p} (\frac{1}{u})[\ln u]^n du = p[\frac{1}{n+1}[\ln u]^{n+1}]^{n+1} = \frac{p}{n+1}[-\ln p]^{n+1} \tag{9}$$

Iterative application of Eq. 8 therefore produces the series

$$F_n(p) = p - p\ln p + p\frac{(\ln p)^2}{2} - p\frac{(\ln p)^3}{6} + p\frac{(\ln p)^4}{24}.... \tag{10}$$

which can be written as

$$F_n(p) = p \sum_{i=0}^{n-1} \frac{(-\ln p)^i}{i!}. \tag{11}$$